Dynamical diffraction effects in STEM orbital angular momentum resolved electron energy-loss magnetic chiral dichroism

Matteo Zanfrognini,[1] Enzo Rotunno,[1] Jan Rusz,[2] Rafal E. Dunin Borkowski,[3] Ebrahim Karimi,[4] Stefano Frabboni,[1,5] and Vincenzo Grillo[1]

[1]*CNR-NANO Via G. Campi 213/a, I-41125 Modena, Italy*

[2]*Department of Physics and Astronomy, Uppsala University, Box 530, S-751 21 Uppsala, Sweden*

[3]*Ernst Ruska-Centre for Microscopy and Spectroscopy with Electrons and Peter Grünberg Institute, Forschungszentrum Jülich, 52425 Jülich, Germany*

[4]*Department of Physics, University of Ottawa, 150 Louis Pasteur, Ottawa, Ontario K1N 6N5, Canada*

[5]*Dipartimento FIM, Università di Modena e Reggio Emilia, Via G. Campi 213/a, I-41125 Modena, Italy*

(Received 4 December 2019; revised 12 August 2020; accepted 28 October 2020; published 17 November 2020)

In this paper, we explore the properties of dynamical diffraction coefficients in orbital angular momentum resolved electron energy-loss magnetic chiral dichroism spectra, in a scanning transmission electron microscopy setup. We demonstrate that for basic zone axis geometries with fourfold or threefold symmetry the coefficients are constrained to have simplified forms. By exploiting these properties, we show how a dichroism spectrum accessible using this technique is only weakly dependent on sample thickness and, more generally, on dynamical diffraction effects. Our results indicate that in such cases it is possible to determine the orbital and spin components of atomic magnetic moments approximately from experimental spectra without the need for additional dynamical diffraction calculations.

DOI: 10.1103/PhysRevB.102.184420

I. INTRODUCTION

Since the work of Schattschneider and colleagues [1], electron energy-loss magnetic chiral dichroism (EMCD) has attracted the attention of many researchers in the field of electron microscopy because of its potential for providing information about the magnetic properties of materials with subnanometric spatial resolution. As in the case of x-ray magnetic circular dichroism [2,3], sum rules for EMCD, which were derived independently by Calmels *et al.* [4] and Rusz *et al.* [5], in principle, permit quantification of the orbital (m_{orb}) and spin (m_s) components of the magnetic moment per atom in a sample by relating these material-specific properties to the experimentally accessible signal. In this way, a quantitative description of the magnetic properties of crystals with close-to-atomic resolution may be possible. However, the practical application of these rules is complicated by the effects of dynamical diffraction, which introduce thickness-dependent effects, which are normally evaluated by using separate dynamical calculations.

In our recent work [6], we proposed to perform orbital angular momentum (OAM) resolved scanning transmission electron microscopy (STEM) EMCD to probe the magnetic properties of crystalline materials that are oriented along high symmetry directions. In this proposed experiment, both the energy and the OAM spectra [7] of the electrons that experienced a core-loss process are measured. Differences between inelastic signals for OAM values of $+\hbar$ and $-\hbar$ are expected for magnetic materials, thereby providing access to these material properties with atomic spatial resolution.

In the present work, we analyze the dependence of OAM-resolved EMCD spectra on the dynamical diffraction of electrons in a magnetic material, with reference to relevant experimental parameters such as sample thickness and probe convergence semiangle, on the assumption that a convergent electron beam is focused onto an atomic column, with the sample oriented in a high symmetry direction.

Our results show that for magnetic crystals with threefold or fourfold rotational symmetries of zone axes it is possible to derive relations between these dynamical coefficients. When combined with specific experimental configurations, they provide the possibility to obtain dichroism signals that are only weakly dependent on dynamical diffraction effects.

This behavior is clearly different from conventional EMCD, where the dichroism signal is generally strongly dependent on dynamical diffraction effects. As pointed out by Rusz *et al.* [8], as a result of dynamical diffraction effects such a signal can become zero for certain sample thicknesses despite a nonzero magnetization of the sample, complicating direct evaluation of the quantities m_{orb}, m_s directly from experimental spectra.

In practice, this situation introduces a considerable advantage when compared with conventional EMCD schemes, since, to a large extent, OAM decomposition on the detector can be directly (i.e., nearly without additional parameter estimation) related to single-atom OAM differential cross sections. As pointed out by Rusz *et al.* [5], single atom cross sections can be interpreted directly in terms of atomic properties such as orbital and spin components of atomic magnetic moments.

In addition, we show how the approach described here can be used to predict, at least qualitatively, characteristics of dynamical coefficients that appear in OAM-resolved loss spectra when the crystal under study does not possess these specific symmetries.

This article is organized as follows. In Sec. II, we briefly summarize the dependence of OAM-resolved EMCD spectra on dynamical coefficients presented in Ref. [6]. In Sec. III, we discuss the properties of the dynamical coefficients introduced in Sec. II for crystals that have specific rotational symmetries. In Sec. IV, we test the relations derived in Sec. III by computing them for different materials and experimental configurations. Furthermore, we discuss how dynamical effects can influence an experimentally-accessible dichroism function and how they enter relations between OAM-resolved electron energy loss spectra and $m_{\rm orb}$, m_s.

II. THEORY

The experimental quantity that can be evaluated directly through the combined action of an OAM sorter [7] and an energy spectrometer in the TEM is the OAM-resolved loss function $I_\beta(\ell, \Delta E)$, which can be formally defined as [6,9,10]

$$I_\beta(\ell, \Delta E) = \int_0^{\frac{2\pi\beta}{\lambda}} I(\ell, k, \Delta E) dk = \int_0^{\frac{2\pi\beta}{\lambda}} \mathrm{Tr}[\hat{\rho}_f \hat{P}_{\ell\Delta E}(k)] dk, \tag{2.1}$$

where $\hat{\rho}_f$ is the density matrix of electrons inelastically scattered by the sample (the subscript f indicates that this is the final electron density matrix, i.e., at the exit surface of the material) and $\hat{P}_{\ell\Delta E}(k)$ is a projector over states $|\ell, k, \Delta E\rangle$ having OAM equal to $\hbar\ell$ along the z axis (the TEM optical axis) and energy $E = E_0 - \Delta E$, where E_0 is the energy of the incoming electron beam.

Physically, Eq. (2.1) describes both inelastic events occurring in the material and postanalysis performed by the combined action of energy and OAM spectrometers. As pointed out in Ref. [10], the density matrix $\hat{\rho}_f$ represents an incoherent sum of partial waves describing electrons that experienced an inelastic process involving magnetic atoms of interest in the sample. At the same time, the operator $\hat{P}_{\ell\Delta E}$ mathematically translates the action of an ideal energy-OAM spectrometer, i.e., it projects each partial wave with energy $E = E_0 - \Delta E$ onto a basis of eigenstates of the orbital angular momentum along z and provides the weight of the component with OAM equal to $\ell\hbar$. The integral over k underlines the fact that, in our setup of OAM-energy measurement, information about the radial state is lost. In the following description, we choose Bessel beams as eigenstates of the OAM operator (i.e., $|\ell, k, \Delta E\rangle$), for which the radial quantum number k corresponds to the electron scattering wave vector in the x-y plane, which is integrated up to the collection semiangle β of the OAM spectrometer. If λ is the electron de Broglie wavelength, then $\lambda k/2\pi$ represents scattering angle, which is given in units of mrad below.

Assuming the validity of the dipolar approximation [6], taking the material magnetization to be saturated along the z axis and considering paraxial conditions for the incoming electrons, it is possible to write $I(\ell, k, \Delta E)$ in Eq. (2.1) as

$$I(\ell, k, \Delta E) = \sum_{i,j}^{x,y,z} N_{ij}(\Delta E) \sum_{\boldsymbol{a}} X^{ij}_{\boldsymbol{a}}(\ell, k) + M(\Delta E) \sum_{\boldsymbol{a}} S^z_{\boldsymbol{a}}(\ell, k), \tag{2.2}$$

where $N_{ij}(\Delta E)$ and $M(\Delta E)$ only depend on the electronic properties of the material and, respectively, describe the nonmagnetic and magnetic contributions to the loss spectrum.

According to this notation, whereas the nonmagnetic part $\mathbb{N}$ is a symmetrical 3×3 matrix, the magnetic component $\boldsymbol{M}$, which should be a vector, is constrained to a single z component because of the assumed vertical magnetization. Summations over atomic positions $\boldsymbol{a}$ are restricted to magnetic atoms that give rise to the energy losses ΔE in which we are interested. We point out here that Eq. (2.2) is only strictly valid if the magnetic atoms of interest in the sample are symmetrically equivalent to one another. Otherwise, a dependency on $\boldsymbol{a}$ should also appear in $N_{ij}(\Delta E)$ and $M(\Delta E)$.

The functions $X^{ij}_{\boldsymbol{a}}(\ell, k)$ and $S^z_{\boldsymbol{a}}(\ell, k)$ define the effects of dynamical diffraction of the electron beam in the sample. They can be written in terms of other functions that are directly related to dynamical diffraction of the incoming and outgoing beams in the crystal, i.e.,

$$X^{ii}_{\boldsymbol{a}}(\ell, k) = |Q_i(\ell, k; \boldsymbol{a})|^2, \tag{2.3a}$$

$$X^{ij}_{\boldsymbol{a}}(\ell, k) = 2\mathrm{Re}[Q_i(\ell, k; \boldsymbol{a}) Q^*_j(\ell, k; \boldsymbol{a})], \tag{2.3b}$$

$$S^z_{\boldsymbol{a}}(\ell, k) = -2\mathrm{Im}[Q_x(\ell, k; \boldsymbol{a}) Q^*_y(\ell, k; \boldsymbol{a})], \tag{2.3c}$$

where we have defined the three-component function

$$Q_i(\ell, k; \boldsymbol{a}) = \sigma \int d\boldsymbol{k}_1 \int d\boldsymbol{k}_2 D^*(\boldsymbol{k}_1; \ell, k) C(\boldsymbol{k}_2) \frac{\tilde{q}_i}{\tilde{q}^2} e^{i(\boldsymbol{k}_1 - \boldsymbol{k}_2)\cdot\boldsymbol{a}} \tag{2.4}$$

for $i, j = x, y, z$, and $\tilde{\boldsymbol{q}} = [k_1^x - k_2^x,\ k_1^y - k_2^y, q_{\Delta E}]$, while $q_{\Delta E}$ is a term that depends on electron probe energy (here, 300 keV) and on the energy lost in a single inelastic event [10]. $C(\boldsymbol{k})$ and $D(\boldsymbol{k}; \ell, k)$ are, respectively, three-dimensional (3D) Fourier transforms of the incoming beam propagating inside the crystal and of a Bessel beam (with orbital angular momentum $\hbar\ell$ along z and transverse wave vector k) back-propagating in the sample, i.e.,

$$C(\boldsymbol{k}) = \int d\boldsymbol{r} e^{-i\boldsymbol{k}\cdot\boldsymbol{r}} \langle \boldsymbol{r}|\hat{U}|\phi_{\rm inc}\rangle, \tag{2.5a}$$

$$D(\boldsymbol{k}; \ell, k) = \int d\boldsymbol{r} e^{-i\boldsymbol{k}\cdot\boldsymbol{r}} \langle \boldsymbol{r}|\hat{U}^+|\psi(\ell, k)\rangle. \tag{2.5b}$$

In these expressions, $\hat{U}(\hat{U}^+)$ is the evolution operator defined in Eq. (3) of Ref. [10], which propagates (back-propagates) the incoming wave function (the Bessel beam) along z in the crystal. $|\phi_{\rm inc}\rangle$ ($|\psi(\ell, k)\rangle$) is a quantum mechanical state, such that the scalar product $\langle \boldsymbol{r}_\perp|\phi_{\rm inc}\rangle = \phi_{\rm inc}(\boldsymbol{r}_\perp)$ ($\langle \boldsymbol{r}_\perp|\psi(\ell, k)\rangle = \psi_\ell(\boldsymbol{r}_\perp; k)$) corresponds to the position representation of the wave function of the electron beam at the entrance plane of the sample (the Bessel beam at the exit plane of the crystal). Here, $\boldsymbol{r}_\perp = (x, y)$, while $\boldsymbol{r} = (x, y, z)$. As shown in Refs. [6,10], the back-propagating Bessel beams

formally appear to represent the action of the OAM spectrometer.

In simplified terms, $\boldsymbol{Q}$ calculates, for each magnetic atom $\boldsymbol{a}$, how much of the impinging probe (dynamically propagated to the atom) is transferred to a given final state (in this case, Bessel beam waves) back-propagated to the same atom after dipolar inelastic scattering.

Integrating Eq. (2.2) over scattering angle $\lambda k/2\pi$ in the limit $[0, \beta]$, the OAM-resolved loss function can be written

$$I_\beta(\ell, \Delta E) = \sum_{i,j}^{x,y,z} N_{ij}(\Delta E) \sum_{\boldsymbol{a}} F_{\boldsymbol{a}}^{ij}(\ell, \beta) + M(\Delta E) \sum_{\boldsymbol{a}} \tilde{S}_{\boldsymbol{a}}^{z}(\ell, \beta), \tag{2.6}$$

where

$$F_{\boldsymbol{a}}^{ij}(\ell, \beta) = \int_0^{\frac{2\pi\beta}{\lambda}} X_{\boldsymbol{a}}^{ij}(\ell, k) k dk, \tag{2.7a}$$

and

$$\tilde{S}_{\boldsymbol{a}}^{z}(\ell, \beta) = \int_0^{\frac{2\pi\beta}{\lambda}} S_{\boldsymbol{a}}^{z}(\ell, k) k dk. \tag{2.7b}$$

We point out here that the functions $F_{\boldsymbol{a}}^{ij}$ and $\tilde{S}_{\boldsymbol{a}}^{z}$ [just as for their not-integrated counterparts $X_{\boldsymbol{a}}^{ij}(\ell, k)$ and $S_{\boldsymbol{a}}^{z}(\ell, k)$] depend on the label $\boldsymbol{a}$, as they represent the contribution of each magnetic atom at position $\boldsymbol{a}$ to that dynamical coefficient. If the index $\boldsymbol{a}$ is omitted, then we are considering a sum over all magnetic atoms of that type in the sample, i.e., for example, $F^{ij}(\ell, \beta) = \sum_{\boldsymbol{a}} F_{\boldsymbol{a}}^{ij}(\ell, \beta)$.

We note here that the STEM probe is always assumed to be centered on a specific atomic column, located at (0,0), which contains magnetic atoms. This choice is rationalized as follows. First, as stated by Schachinger *et al.* [11], inelastic scattering localizes the scattered wave mainly on the column, almost regardless of the initial condition. Second, it helps that a small shift cannot induce an $\ell = \pm 1$ asymmetry in the OAM decomposition of the initial probe with respect to the origin [12] and, although still important, it does not directly affect the dichroism. Finally, we have used simulations [6] to demonstrate the possibility of atomically resolved EMCD. The simulations indicated a smooth change of the EMCD signal as a function of off-column shift.

This statement is in apparent contradiction to the large effect of such a shift on EMCD when using a vortex probe [13]. However, as a result of the absence of time invariance in inelastic scattering, this situation cannot be considered to be the inverse of the present experiment.

III. EFFECTS OF CRYSTAL SYMMETRIES ON DYNAMICAL COEFFICIENTS

In this section, we derive analytical relations between dynamical coefficients appearing in Eq. (2.3) in the presence of crystal symmetries, which can be formally represented by a unitary symmetry operator $\hat{A}$, such that $\hat{A}|\boldsymbol{r}\rangle = |\bar{\bar{A}}\boldsymbol{r}\rangle$, where $\bar{\bar{A}}$ is a matrix associated with a symmetry operation in real space. If we assume that the crystal is invariant under this symmetry operation, then $[\hat{V}, \hat{A}] = 0$ (where $\hat{V}$ is the crystal potential), so $[\hat{U}, \hat{A}] = [\hat{U}^+, \hat{A}] = 0$. Focusing on the matrix element in Eq. (2.5b) we can write

$$\begin{aligned}\langle \boldsymbol{r}|\hat{U}^+|\psi(\ell, k)\rangle &= \langle \boldsymbol{r}|\hat{A}^+\hat{U}^+\hat{A}|\psi(\ell, k)\rangle \\ &= \left\langle \bar{\bar{A}}\boldsymbol{r}|\hat{U}^+ \int d\boldsymbol{r}_\perp \hat{A}|\boldsymbol{r}_\perp\right\rangle \langle \boldsymbol{r}_\perp|\psi(\ell, k)\rangle,\end{aligned}$$

where $\hat{A}|\boldsymbol{r}_\perp\rangle = |\bar{\bar{A}}_\perp \boldsymbol{r}_\perp\rangle$, $\bar{\bar{A}}_\perp$ is the matrix obtained from $\bar{\bar{A}}$ by removing the row and the column associated with z.

The symmetry operators that are considered in the present work always satisfy the relation

$$\langle \bar{\bar{A}}_\perp^{-1} \boldsymbol{r}_\perp|\psi(\ell, k)\rangle = e^{i\gamma_\ell}\langle \boldsymbol{r}_\perp|\psi(p\ell, k)\rangle, \tag{3.1}$$

where $p = \pm 1$ and γ_ℓ is a real number that depends on the Bessel beam OAM index ℓ.

Therefore, we can write

$$\langle \boldsymbol{r}|\hat{U}^+|\psi(\ell, k)\rangle = e^{i\gamma_\ell}\langle \bar{\bar{A}}\boldsymbol{r}|\hat{U}^+|\psi(p\ell, k)\rangle. \tag{3.2}$$

As the incident beam is a standard beam, which is assumed not to have aberrations, its OAM decomposition can be assumed to be composed only of the $\ell = 0$ component.

In this case, it can be stated immediately that

$$\langle \boldsymbol{r}|\hat{U}|\phi_{\text{inc}}\rangle = \langle \bar{\bar{A}}\boldsymbol{r}|\hat{U}|\phi_{\text{inc}}\rangle. \tag{3.3}$$

By making use of Eqs. (3.1) and (3.2), Eqs. (2.5) can be rewritten in the form

$$C(\boldsymbol{k}) = \int d\boldsymbol{r} e^{-i\boldsymbol{k}\cdot\boldsymbol{r}}\langle \bar{\bar{A}}\boldsymbol{r}|\hat{U}|\phi_{\text{inc}}\rangle = \int d\boldsymbol{r}' e^{-i(\bar{\bar{A}}\boldsymbol{k})\cdot\boldsymbol{r}'}\langle \boldsymbol{r}'|\hat{U}|\phi_{\text{inc}}\rangle, \tag{3.4a}$$

$$\begin{aligned}D(\boldsymbol{k}) &= e^{i\gamma_\ell}\int d\boldsymbol{r} e^{-i\boldsymbol{k}\boldsymbol{r}}\langle \bar{\bar{A}}\boldsymbol{r}|\hat{U}^+|\psi(p\ell, k)\rangle \\ &= e^{i\gamma_\ell}\int d\boldsymbol{r}' e^{-i(\bar{\bar{A}}\boldsymbol{k})\cdot\boldsymbol{r}'}\langle \boldsymbol{r}'|\hat{U}^+|\psi(p\ell, k)\rangle,\end{aligned} \tag{3.4b}$$

from which it is possible to infer that $C(\boldsymbol{k}) = C(\bar{\bar{A}}\boldsymbol{k})$ and $D(\boldsymbol{k};\ \ell, k) = e^{i\gamma_\ell} D(\bar{\bar{A}}\boldsymbol{k};\ p\ell, k)$.

Equation (2.4) can then be rewritten in the form

$$\begin{aligned}Q_i(\ell, k; \boldsymbol{a}) = \sigma \int d\boldsymbol{k}_1 \int d\boldsymbol{k}_2 e^{-i\gamma_\ell} D^*(\bar{\bar{A}}\boldsymbol{k}_1;\ p\ell, k) \\ \times C(\bar{\bar{A}}\boldsymbol{k}_2)\frac{\tilde{q}_i}{\tilde{q}^2} e^{i(\boldsymbol{k}_1 - \boldsymbol{k}_2)\cdot\boldsymbol{a}}.\end{aligned}$$

By making the variable substitution $\boldsymbol{k}'_{1,2} = \bar{\bar{A}}\boldsymbol{k}_{1,2}$, and by making use of the fact that $(\boldsymbol{k}_1 - \boldsymbol{k}_2)\cdot\boldsymbol{a} = \bar{\bar{A}}^{-1}(\boldsymbol{k}'_1 - \boldsymbol{k}'_2)\cdot\boldsymbol{a} = (\bar{\bar{A}}\boldsymbol{a})\cdot(\boldsymbol{k}'_1 - \boldsymbol{k}'_2)$, it is possible to write

$$\boldsymbol{Q}(\ell, k; \boldsymbol{a}) = e^{-i\gamma_\ell}[\bar{\bar{A}}_0^{-1}\boldsymbol{Q}(p\ell, k; \bar{\bar{A}}\boldsymbol{a})], \tag{3.5}$$

where $\boldsymbol{Q}(\ell, k; \boldsymbol{a}) = [Q_x(\ell, k; \boldsymbol{a}), Q_y(\ell, k; \boldsymbol{a}), Q_z(\ell, k; \boldsymbol{a})]$ and $\bar{\bar{A}}_0$ is a matrix obtained from $\bar{\bar{A}}$ by setting $\bar{\bar{A}}_{(3,3)} = 1$ and $\bar{\bar{A}}_{(3,i)} = \bar{\bar{A}}_{(i,3)} = 0$, for $i = 1, 2$, as $\tilde{q}_z$ is fixed to $q_{\Delta E}$. In this way, it is possible to relate the quantities $Q_i(\ell, k; \boldsymbol{a})$, for a given specific symmetry $\hat{A}$ that satisfies Eq. (3.1).

We will now use Eq. (3.5) to understand the properties of the dynamical coefficients under rotational symmetries.

A. Rotational symmetry around an atomic column

We begin by considering a crystal that is invariant under rotation by an angle $\alpha \in \{\frac{\pi}{2}, \frac{2\pi}{3}, \pi\}$ around an atomic column located at (0,0) in the x-y plane, on which an electron probe is focused. These cases correspond to fourfold, threefold, and twofold rotational symmetries.

In this case, $\bar{\bar{A}} = \bar{\bar{A}}_\alpha$ corresponds to a matrix associated with a rotation along z, so that $\bar{\bar{A}} = \bar{\bar{A}}_0$. Following rotation by an angle α around z,

$$\langle \bar{\bar{A}}_\perp{}^{-1} \boldsymbol{r}_\perp | \psi(\ell, k)\rangle = J_\ell(k|\boldsymbol{r}_\perp|) e^{i\ell\phi'} = e^{-i\ell\alpha} \langle \boldsymbol{r}_\perp | \psi(\ell, k)\rangle,$$

where $\phi' = \phi - \alpha$ is the transformed azimuthal angle. For these transformations, we find $p = 1$ and $\gamma_\ell = -\ell\alpha$.

Equation (3.5) can be used to obtain relations between the coefficients $Q_i(\ell, k; \boldsymbol{a})$, for $i = x, y, z$. We first discuss the case of $\boldsymbol{a}$ belonging to column (0,0). We then focus on the case of $\boldsymbol{a}$ belonging to a different atomic column. We highlight the fact that, when the dynamical coefficients Q_i are considered for atoms on the (0,0) column, this means that we are taking into account the contribution to the loss signal due to atoms on that column. However, dynamical diffraction of both the incoming beam and the back-propagating vortices from all of the (magnetic and nonmagnetic) atoms in the sample is fully taken into account.

As a magnetic atom on the column transforms into itself under such a rotation, in this case $\bar{\bar{A}}\boldsymbol{a} = \boldsymbol{a}$, where $\boldsymbol{a}$ corresponds to $(0, 0, a_z)$. We therefore find that $\boldsymbol{Q}(\ell, k; a_z) = e^{i\ell\alpha}[\bar{\bar{A}}_0{}^{-1} \boldsymbol{Q}(\ell, k; a_z)]$.

By reversing this equation, we find (for $\alpha \neq \pi$) that

$$Q_x(\ell, k; a_z) = \frac{e^{i\ell\alpha} \sin\alpha}{1 - e^{i\ell\alpha}\cos\alpha} Q_y(\ell, k; a_z), \tag{3.6a}$$

$$Q_z(\ell, k; a_z) = e^{i\ell\alpha} Q_z(\ell, k; a_z). \tag{3.6b}$$

Starting from Eq. (3.6b) for $\ell = \pm 1$, we note that $Q_z(\ell, k; a_z)$ is nonzero only if $(1 - e^{\pm i\alpha}) = 0$, which is not possible for the angles considered here. Therefore, the terms $X^{zz}_{a_z}(\ell = \pm 1, k)$ are zero, exactly as the cross terms evaluated for $j = z$, i.e., $X^{iz}_{a_z}(\ell = \pm 1, k) = 0$.

At the same time, according to Eq. (3.6a), $X^{xx}_{a_z}(\ell = \pm 1, k) = X^{yy}_{a_z}(\ell = \pm 1, k)$, for $\alpha \in \{\frac{\pi}{2}, \frac{2\pi}{3}\}$, while from

$$[Q_x(\ell, k; a_z) Q_y^*(\ell, k; a_z)] = \frac{e^{i\ell\alpha} \sin\alpha}{1 - e^{i\ell\alpha}\cos\alpha} |Q_y(\ell, k; a_z)|^2,$$

we immediately find that $X^{xy}_{a_z}(\ell = \pm 1, k) = 0$ together with $S^z_{a_z}(\ell = \pm 1, k) = -2\ell X^{yy}_{a_z}(\ell = \pm 1, k)$, simply using the definitions provided in Eq. (2.3) and finding that the right side of the above expression is imaginary because $\frac{e^{i\ell\alpha}\sin\alpha}{1-e^{i\ell\alpha}\cos\alpha} = \pm i$ for both $\alpha = \frac{\pi}{2}$ and $\alpha = \frac{2\pi}{3}$.

Therefore, for rotation angles $\alpha \in \{\frac{\pi}{2}, \frac{2\pi}{3}\}$, contributions to the dynamical coefficients X^{ij} and S^z from atoms $(0, 0, a_z)$ are either zero or they can be expressed in terms of X^{yy} (or X^{xx}). These results are summarized for convenience as follows:

$$X^{xx}_{a_z}(\ell = \pm 1, k) = X^{yy}_{a_z}(\ell = \pm 1, k), \tag{3.7a}$$

$$X^{zz}_{a_z}(\ell = \pm 1, k) = 0, \tag{3.7b}$$

$$X^{iz}_{a_z}(\ell = \pm 1, k) = 0 \quad \text{for } i = x, y, \tag{3.7c}$$

$$X^{xy}_{a_z}(\ell = \pm 1, k) = 0, \tag{3.7d}$$

$$S^z_{a_z}(\ell = \pm 1, k) = -2\ell X^{yy}_{a_z}(\ell = \pm 1, k). \tag{3.7e}$$

For $\alpha = \pi$, Eq. (3.6a) is not valid. Therefore, it is not possible to generally obtain a relation between $Q_x(\ell, k; a_z)$ and $Q_y(\ell, k; a_z)$. Consequently, relations similar to Eqs. (3.7a), (3.7d), and (3.7e) cannot be obtained for this specific rotation angle, whereas Eqs. (3.7b) and (3.7c) are still valid.

We now describe how magnetic atoms outside the (0,0) column contribute to the dynamical coefficients that appear in OAM-resolved loss spectra. We focus on $\frac{2\pi}{3}$-rotational invariant crystals. In Appendix A, we present an analogous reasoning for the other rotational symmetries considered here.

In such a crystalline system, for a magnetic atom in position $\boldsymbol{a}_0$ out away from the (0,0) column, there will be two other atoms of the same type (whose positions are defined in the following as $\boldsymbol{a}_1$ and $\boldsymbol{a}_2$), such that $\boldsymbol{a}_1 = \bar{\bar{A}}\boldsymbol{a}_0$, $\boldsymbol{a}_2 = \bar{\bar{A}}\boldsymbol{a}_1$ and $\boldsymbol{a}_0 = \bar{\bar{A}}\boldsymbol{a}_2$.

By using Eq. (3.5), we can write

$$\begin{aligned}\boldsymbol{Q}(\ell, k; \boldsymbol{a}_1) &= e^{i\ell\frac{2\pi}{3}}[\bar{\bar{A}}^{-1}\boldsymbol{Q}(\ell, k; \bar{\bar{A}}\boldsymbol{a}_1)] = e^{i\ell\frac{2\pi}{3}}[\bar{\bar{A}}^{-1}\boldsymbol{Q}(\ell, k; \boldsymbol{a}_2)] \\ &= e^{i\ell\frac{4\pi}{3}}[\bar{\bar{A}}^{-1}\bar{\bar{A}}^{-1}\boldsymbol{Q}(\ell, k; \boldsymbol{a}_0)],\end{aligned} \tag{3.8a}$$

$$\boldsymbol{Q}(\ell, k; \boldsymbol{a}_2) = e^{i\ell\frac{2\pi}{3}}[\bar{\bar{A}}^{-1}\boldsymbol{Q}(\ell, k; \bar{\bar{A}}\boldsymbol{a}_2)] = e^{i\ell\frac{2\pi}{3}}[\bar{\bar{A}}^{-1}\boldsymbol{Q}(\ell, k; \boldsymbol{a}_0)]. \tag{3.8b}$$

In this way, we can write the functions $\boldsymbol{Q}$ for these atoms in terms of their values computed for only one of them, here chosen to be $\boldsymbol{a}_0$.

Equation (3.8) can be used to compute the sum of the contributions of these atoms to the various dynamical coefficients, i.e.,

$$\begin{aligned}\sum_{\boldsymbol{a}\in\{\boldsymbol{a}_0,\boldsymbol{a}_1,\boldsymbol{a}_2\}} |Q_x(\ell, k; \boldsymbol{a})|^2 &= \frac{3}{2}[|Q_x(\ell, k; \boldsymbol{a}_0)|^2 + |Q_y(\ell, k; \boldsymbol{a}_0)|^2] \\ &= \sum_{\boldsymbol{a}\in\{\boldsymbol{a}_0,\boldsymbol{a}_1,\boldsymbol{a}_2\}} |Q_y(\ell, k; \boldsymbol{a})|^2,\end{aligned} \tag{3.9a}$$

$$2\mathrm{Re}\left[\sum_{\boldsymbol{a}\in\{\boldsymbol{a}_0,\boldsymbol{a}_1,\boldsymbol{a}_2\}} Q_x(\ell, k; \boldsymbol{a}) Q_y{}^*(\ell, k; \boldsymbol{a})\right] = 0, \tag{3.9b}$$

$$\begin{aligned}&-2\mathrm{Im}\left[\sum_{\boldsymbol{a}\in\{\boldsymbol{a}_0,\boldsymbol{a}_1,\boldsymbol{a}_2\}} Q_x(\ell, k; \boldsymbol{a}) Q_y{}^*(\ell, k; \boldsymbol{a})\right] \\ &\quad = -6\mathrm{Im}[Q_x(\ell, k; \boldsymbol{a}_0) Q_y{}^*(\ell, k; \boldsymbol{a}_0)],\end{aligned} \tag{3.9c}$$

$$\sum_{\boldsymbol{a}\in\{\boldsymbol{a}_0,\boldsymbol{a}_1,\boldsymbol{a}_2\}} Q_i(\ell, k; \boldsymbol{a}) Q_z{}^*(\ell, k; \boldsymbol{a}) = 0, \quad i = x, y, \tag{3.9d}$$

$$\sum_{\boldsymbol{a}\in\{\boldsymbol{a}_0,\boldsymbol{a}_1,\boldsymbol{a}_2\}} |Q_z(\ell, k; \boldsymbol{a})|^2 = 3|Q_z(\ell, k; \boldsymbol{a}_0)|^2. \tag{3.9e}$$

Equation (3.9a) indicates that $\sum_{\boldsymbol{a}} X^{xx}_{\boldsymbol{a}}(\ell, k) = \sum_{\boldsymbol{a}} X^{yy}_{\boldsymbol{a}}(\ell, k)$: this is because the magnetic atoms within the (0,0) column provide the same contributions to X^{xx} and X^{yy}, while the sum of the contributions to X^{xx} and X^{yy} from atoms outside the column connected by rotations of $\frac{2\pi}{3}$ are the same.

Second, all of the cross terms are exactly zero. As pointed out above, atoms $(0, 0, a_z)$ do not contribute to X^{ij}, while terms coming from the remaining atoms sum to zero, i.e., their contributions mutually compensate, according to Eqs. (3.9b) and (3.9d). Furthermore, Eq. (3.9e) indicates that the total X^{zz} is expected to be nonzero because of contributions from out-of-column atoms.

Finally, from Eq. (3.9c) it is possible to realize that atoms on columns different from that at (0,0) sum their contributions to S^z, which, therefore, has both on-column and out-of-column terms.

As outlined in Appendix A, analogous conclusions can be drawn for $\alpha = \frac{\pi}{2}$ (apart differences in numerical constants), whereas for $\alpha = \pi$ it is only possible to predict a cancellation of contributions from atoms that are oppositely positioned with respect to the center, to the cross terms X^{iz}, for $i \neq z$.

We note that the results obtained in this section are independent of experimentally tunable parameters, such as STEM probe convergence semiangle, OAM spectrometer collection semiangle, and probe channeling properties along an atomic column, as they are derived only on the basis of symmetry considerations. We will show in Sec. V how an appropriate choice of experimental configuration can be used to provide further simplifications of the results derived here.

B. Relation between $\ell = \pm 1$ dynamical diffraction coefficients

We briefly recall a result already presented in Ref. [6], with regard to the possibility of establishing equalities between the moduli of dynamical diffraction coefficients computed for $\ell = \pm 1$ in the presence of invariance under mirror plane reflection.

More precisely, when a crystal is invariant under mirror reflection with respect to a plane containing the TEM optical axis, i.e.,$(x, y, z) \rightarrow (-x, y, z)$ or $(x, y, z) \rightarrow (x, -y, z)$, we can apply Eq. (3.5) by taking $\gamma_\ell = 0$ and $p = -1$ to find a connection between the functions Q_i computed for $\ell = +1$ and $\ell = -1$. Straightforward calculations demonstrate that $\sum_a X_a^{ii}(\ell, k) = \sum_a X_a^{ii}(-\ell, k)$ $(i = x, y, z)$, $\sum_a S_a^z(\ell, k) = -\sum_a S_a^z(-\ell, k)$ and $\sum_a X_a^{xy}(\ell, k) = -\sum_a X_a^{xy}(-\ell, k)$.

These findings are only determined by symmetry considerations and will be useful in the next sections, when we sum and subtract OAM-resolved EMCD spectra to compute the relative dichroism function.

IV. NUMERICAL CALCULATION OF DYNAMICAL DIFFRACTION COEFFICIENTS IN CRYSTALS WITH ROTATIONAL SYMMETRIES

In this section, we present calculations of dynamical diffraction coefficients discussed in Sec. III for three cases: [001] hcp cobalt, which is $\frac{2\pi}{3}$-rotationally invariant; [001] iron platinum, which has $\frac{\pi}{2}$-rotational symmetry; [110] bcc iron, which has only a twofold rotational axis parallel to the TEM optical axis. The calculations are performed using a modified version of MATS.v2 code [14].

We start from [001] hcp cobalt. We perform calculations for different convergence semiangles of the STEM probe and for two different sample thicknesses of 20 and 40 nm. These values are chosen because, in conventional EMCD, the dichroism signal is expected to decrease by ∼80% on going from a 20-nm-thick to a 40-nm-thick Co crystal. (See Fig. 6 in Ref. [8]). As we discuss in Sec. IV A, for OAM-resolved EMCD the changes in this signal are much smaller with sample thickness.

Figures 1(a) and 1(b) show the quantities $X^{xx}(1, \eta)$ and $X^{yy}(1, \eta)$ plotted as a function of scattering angle $\eta = \lambda k/2\pi$ (where k is the Bessel transverse wave vector) for convergence semiangles (θ) of 10, 16, and 22 mrad for sample thicknesses of 20 and 40 nm. We notice that, independent of θ, the two dynamical coefficients numerically coincide for each value of the scattering angle η, in agreement with the results found in Sec. III. Therefore, in integrated OAM-resolved EMCD spectra it is possible to fix $F^{xx}(1, \beta) = F^{yy}(1, \beta)$ in an exact way.

Figures 1(c) and 1(d) show the ratios $\frac{F^{zz}(1,\beta)}{F^{xx}(1,\beta)}$ computed for different values of θ for sample thicknesses of 20 and 40 nm, respectively. These ratios depend on the parameter θ. Specifically, for $\theta = 16$ mrad this quantity is smaller than for $\theta = 10$ mrad and $\theta = 19$ mrad. In order to further investigate this trend with θ, the insets show averages of the ratios for $\beta \in [5, 20]$ mrad, where these quantities are approximately constant w.r.t. the collection semiangle. For both thicknesses, the averages have minima at $\theta = 16$ mrad, whereas they increase rapidly for smaller values of θ. At the same time, a small increase is observed for larger values of the convergence semiangle.

This behavior can be rationalized by the fact that a 16 mrad probe channels better along the atomic column on which it is located when compared with other beams. As the probability of an inelastic event at a particular atom is proportional to the probe current density at that point, the number of excitations that take place on columns different from that at (0,0) will be small, as will be the value of F^{zz}, which is only derived from inelastic events occurring at these atoms. Quantitatively, separate multislice calculations (not shown here) indicate that for a convergence semiangle of 16 mrad the probe current density on the (0,0) column is almost two orders of magnitude greater than that on a neighboring column, in agreement with the average value of $\frac{F^{zz}(1,\beta)}{F^{xx}(1,\beta)}$ for this value of θ, which is ∼0.017 (0.022) for the 20 nm (40 nm) sample thickness.

These results suggest that, by using probes that show strong channeling along the (0,0) atomic column, it is possible to neglect F^{zz} with respect to F^{xx}. This assumption is reasonable only if an appropriate probe is chosen. For a probe of 7 mrad, on average $F^{zz}(1, \beta)$ can reach values of ∼10% of $F^{xx}(1, \beta)$ for certain values of β. Therefore, neglecting this term in an OAM-resolved loss spectrum is a rather poor approximation.

Figures 1(e) and 1(f) show the ratios $\frac{F^{xz}(1,\beta)}{F^{xx}(1,\beta)}$, $\frac{F^{yz}(1,\beta)}{F^{xx}(1,\beta)}$ and $\frac{F^{xy}(1,\beta)}{F^{xx}(1,\beta)}$ evaluated for $\theta = 16$ mrad. These ratios also have the same trends when they are computed for different values of θ, i.e., they are equal to zero within numerical accuracy (this result is further highlighted in the insets, which show averages of these quantities for the interval $\beta \in [5, 20]$ mrad for the different probes, of on average below 0.002). These results agree with the predictions outlined in Sec. III that the cross terms are zero, as they have no contributions from the (0,0) atoms, while the terms from neighboring columns

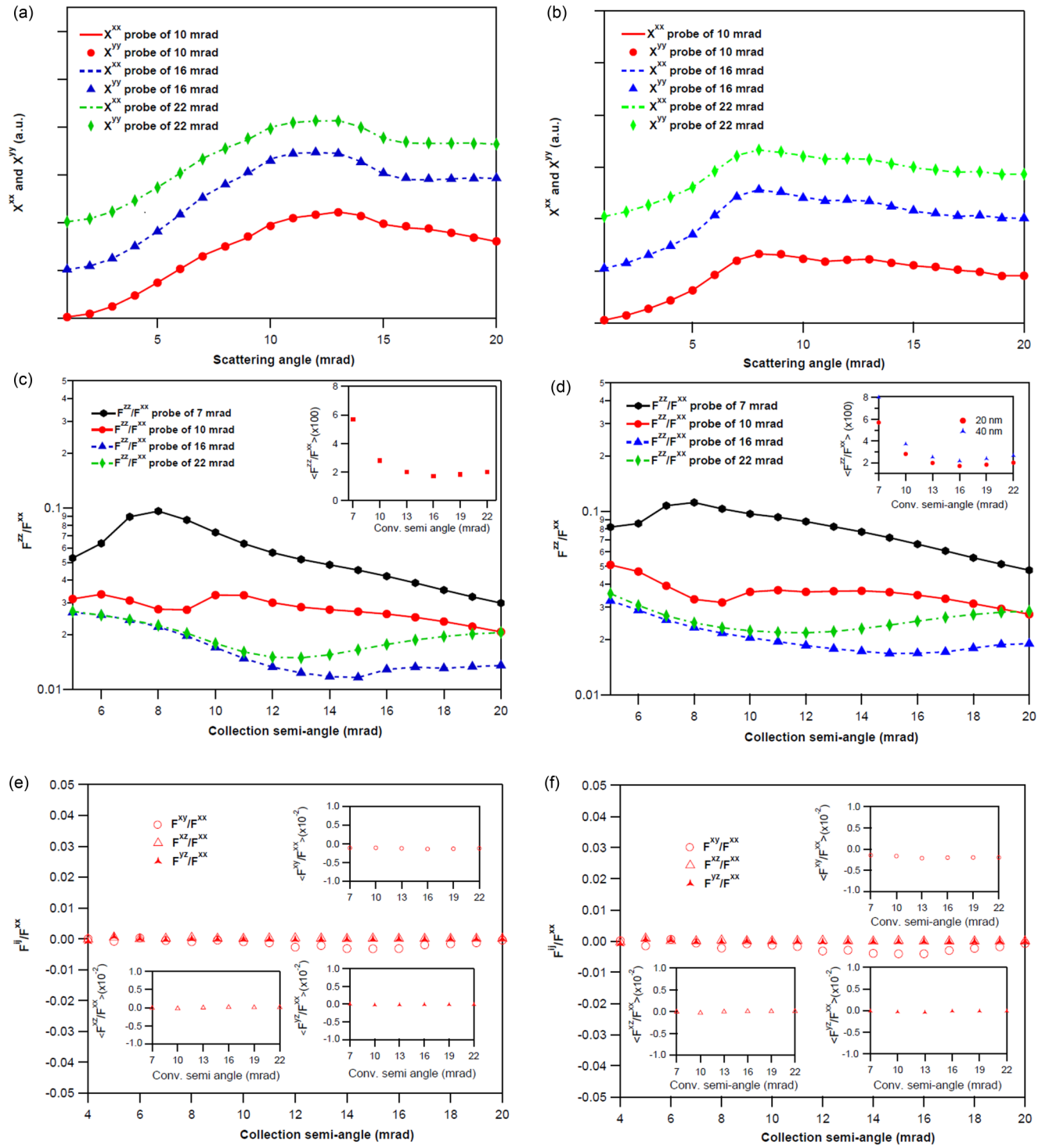

FIG. 1. Dynamical diffraction coefficients computed for hcp [001] cobalt samples of thickness (a),(c),(e) 20 nm and (b),(d),(f) 40 nm. (a) and (b) show the functions X^{xx} and X^{yy} as a function of scattering angle evaluated for $\ell = 1$ and for STEM probe convergence semiangles of 10, 16, and 22 mrad. The results for 16 and 22 mrad are shifted upward in intensity to improve readability. (c) and (d) show the ratios F^{zz}/F^{xx} for different probes (the y axis is on a log scale). The insets show averages of these ratios for collection semiangles $\beta \in [5,20]$ mrad for STEM convergence semiangles in the interval [7,22] mrad. (e) and (f) show the ratios F^{xy}/F^{xx}, F^{xz}/F^{xx} and F^{yz}/F^{xx} for a probe of 16 mrad. The insets show their averages for collection semiangles $\beta \in [5,20]$ mrad for the same convergence semiangle as in (c) and (d).

cancel with each other. These compensating effects are further clarified in Appendix B, which shows the contributions of these cross-terms of each nearest neighboring column to that at (0,0).

Similar results can be obtained for a crystal that has $\frac{\pi}{2}$-rotational symmetry, as observed for iron platinum. Figures 2(a)–2(f) show the same quantities as for hcp cobalt, from

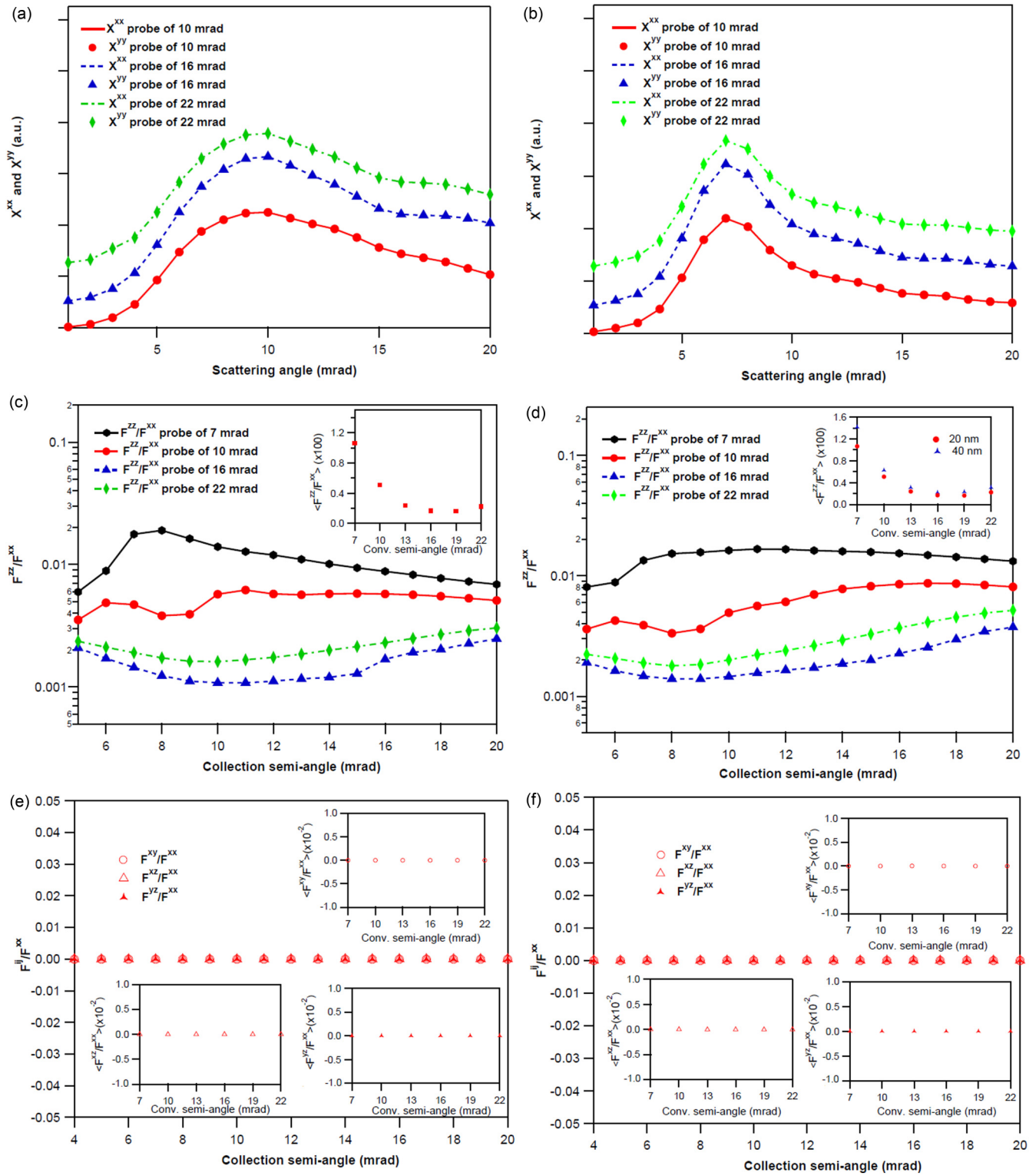

FIG. 2. As for Fig. 1, but for an [001] FePt crystal for sample thicknesses of (a),(c),(e) 20 nm and (b),(d),(f) 40 nm.

which we can immediately draw the same conclusions as for the previous case.

As an additional comment, we note that for FePt the ratios $\frac{F^{zz}(1,\beta)}{F^{xx}(1,\beta)}$ are generally smaller than those for hcp cobalt (also below 0.01) for the same values of θ, as columns nearest to that on which the probe is located are only made of Pt atoms, while Fe atoms are on further columns, where the probe current density is expected to be much smaller for a well-channeling probe.

As a final example, we consider [110] bcc iron, which is invariant only under a π rotation along an atomic column. Figures 3(a)–3(d) show dynamical coefficients computed for

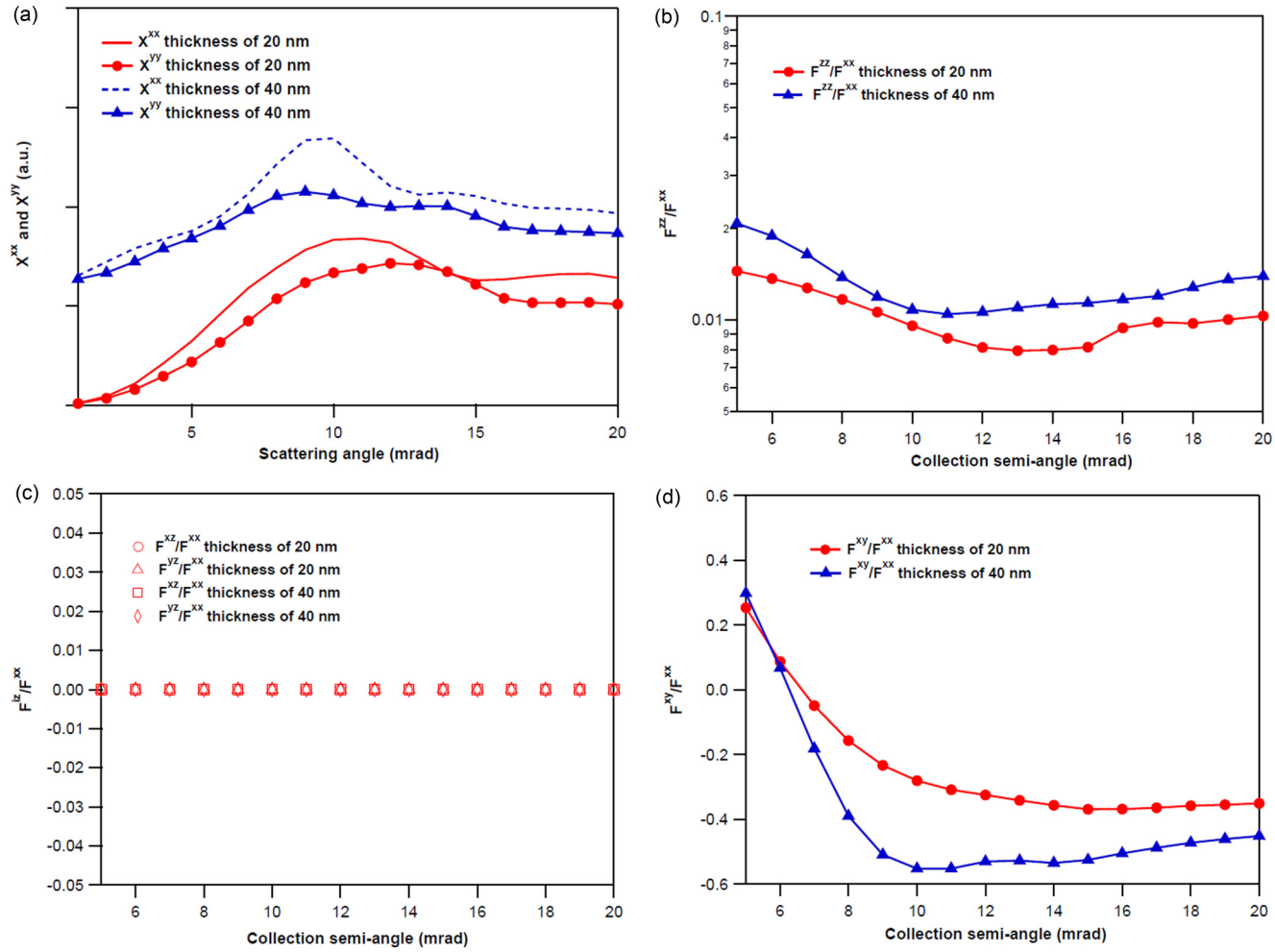

FIG. 3. Dynamical diffraction coefficients calculated for a convergence semiangle of 16 mrad for bcc Fe oriented along the [110] direction for sample thicknesses of 20 nm and 40 nm. (a) shows the quantities X^{xx} and X^{yy} which are shown as a function of scattering angle for $\ell = 1$. The data for a 40-nm-thick crystal are shifted rigidly upwards to make the figure more readable. (b) shows the ratio F^{zz}/F^{xx} evaluated for the two sample thicknesses (again for $\ell = 1$) as a function of collection semiangle β. (c) shows ratios between the cross terms F^{iz} and F^{xx}. (d) shows the ratio F^{xy}/F^{xx} for the two sample thicknesses.

sample thicknesses of 20 and 40 nm. In order to simplify the treatment, we present calculations only for a well-channeling probe of 16 mrad.

Figure 3(a) reveals different trends for $X^{xx}(1,\eta)$ and $X^{yy}(1,\eta)$, which also change with sample thickness. Figure 3(b) shows the ratios $\frac{F^{zz}(1,\beta)}{F^{xx}(1,\beta)}$, which are again small [$F^{zz}(1,\beta)$ can be reduced to about 1–2% $F^{xx}(1,\beta)$], as for π-rotational invariance the only contributions to F^{zz} come from magnetic atoms on columns neighboring that at (0,0), again justifying the nonzero value. For probes with smaller values of θ, we observe a larger ratio as the current density on the neighboring columns is greater, as in the two previous cases.

Figure 3(c) shows the ratios $\frac{F^{xz}(1,\beta)}{F^{xx}(1,\beta)}$, $\frac{F^{yz}(1,\beta)}{F^{xx}(1,\beta)}$, while Fig. 3(d) shows $\frac{F^{xy}(1,\beta)}{F^{xx}(1,\beta)}$. The first two terms are zero for the reasons described above for cobalt and iron platinum, while $\frac{F^{xy}(1,\beta)}{F^{xx}(1,\beta)}$ is now nonzero. The relations between $Q_x(\ell,k;\boldsymbol{a})$ and $Q_y(\ell,k;\boldsymbol{a})$ in presence of this rotational symmetry depend strongly on crystal anisotropy in the x and y directions, which is specific to each system. In contrast to the specific situation for $\frac{\pi}{2}$ and $\frac{2\pi}{3}$ rotational symmetry, it is not possible to generally describe the effects of dynamical diffraction in dichroic spectra. Instead, careful numerical analysis has to be performed for each π-invariant system under study. Nevertheless, in Sec. I of the Supplementary Material [15] we discuss selected examples from this category, in order to show how it is possible to use the reasoning outlined in this work to predict, at least qualitatively, features of the dynamical diffraction coefficients in π rotationally invariant systems.

A. OAM-resolved dichroic spectra for $\frac{\pi}{2}$ and $\frac{2\pi}{3}$ rotationally symmetric crystals

Based on the analytical results obtained in Sec. III and on the numerical simulations in Sec. IV, we can derive a simplified form for OAM-resolved loss spectra for $\ell = \pm 1$, in case of crystals that are invariant under a rotation of $\frac{\pi}{2}$ or $\frac{2\pi}{3}$ around an atomic column. We can then write

$$I_\beta(\ell=\pm1,\Delta E) \approx [N_{xx}(\Delta E)+N_{yy}(\Delta E)]F^{xx}(\ell=\pm1,\beta) + M(\Delta E)\tilde{S}^z(\ell=\pm1,\beta). \quad (4.1)$$

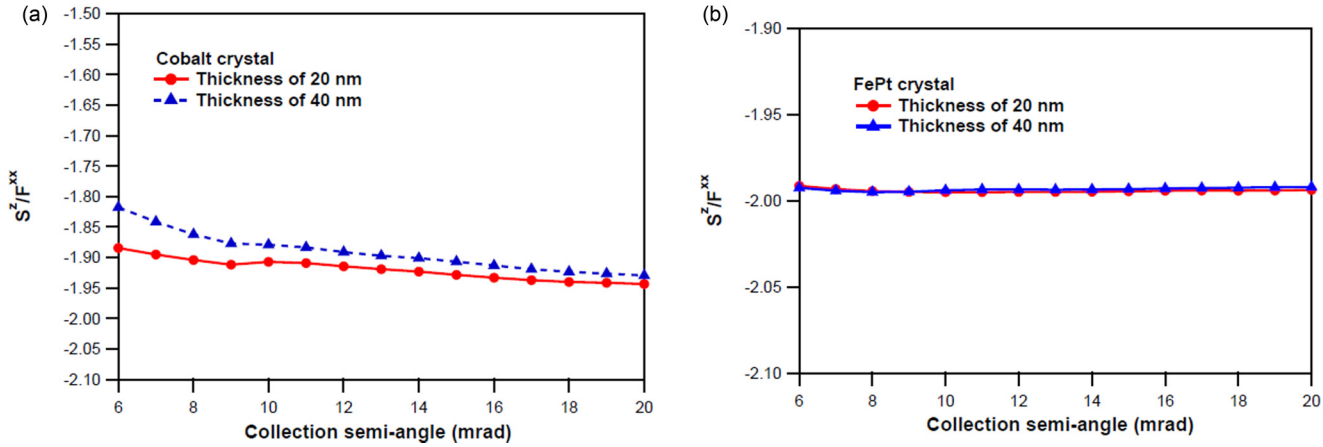

FIG. 4. Ratios $\tilde{S}^z/F^{xx}$ computed for $\ell = 1$ and for a probe convergence semiangle of 16 mrad for (a) [001] cobalt and (b) [001] FePt.

We recall here that the relations $F^{xx}(\ell = \pm 1, \beta) = F^{yy}(\ell = \pm 1, \beta)$, $F^{iz}(\ell = \pm 1, \beta) = 0$ (for $i = x, y$) and $F^{xy}(\ell = \pm 1, \beta) = 0$ are valid for symmetry reasons, independent of the probe characteristics, whereas the assumption $F^{zz}(\ell = \pm 1, \beta) \approx 0$ is valid only if the STEM probe strongly channels along the atomic column on which it is focused.

For a sample that is mirror-symmetric w.r.t. the x-z or y-z planes, in Sec. III B we derived the relations $F^{xx}(\ell, \beta) = F^{xx}(-\ell, \beta)$, together with $\tilde{S}^z(\ell, \beta) = -\tilde{S}^z(-\ell, \beta)$. The relative dichroism function defined in Ref. [6] is then given by the expression

$$D(\beta, \Delta E) = \frac{I_\beta(1, \Delta E) - I_\beta(-1, \Delta E)}{I_\beta(1, \Delta E) + I_\beta(-1, \Delta E)} = \frac{\tilde{S}^z(1, \beta)}{F^{xx}(1, \beta)} \frac{M(\Delta E)}{[N_{xx}(\Delta E) + N_{yy}(\Delta E)]}, \quad (4.2)$$

which depends on dynamical diffraction only through $\frac{\tilde{S}^z(1,\beta)}{F^{xx}(1,\beta)}$, whereas the ratio $\frac{M(\Delta E)}{[N_{xx}(\Delta E)+N_{yy}(\Delta E)]}$ is determined solely by the magnetic properties of the sample.

Figure 4(a) shows $\frac{\tilde{S}^z(1,\beta)}{F^{xx}(1,\beta)}$ for an [001] hcp cobalt crystal of thickness 20 and 40 nm for a convergence semiangle of 16 mrad and for collection semiangles $\beta \in [6, 20]$ mrad, which are accessible experimentally using presently-available OAM spectrometers [7]. Figure 4(b) shows the same quantities evaluated for 20-nm-thick and 40-nm-thick [001] FePt samples.

In both cases, the ratios vary slowly as a functions of β and are close to -2. For a 20-nm-thick Co sample, the ratio takes values between -1.88 and -1.94, while for a 40-nm-thick sample it takes values between -1.82 and -1.93. Therefore, the difference from the limiting value of -2 is 3–6% for the 20-nm-thick sample and 4–9% for the 40-nm-thick sample, with a weak dependence on collection semiangle β.

For FePt, the ratio is much closer to -2 for both thicknesses, varying between -1.98 and -1.99, with that for the 40-nm-thick crystal being slightly larger than that for the 20-nm-thick crystal.

This limiting value was effectively predicted in Sec. III, after demonstrating analytically that $\tilde{S}^z(1, \beta)$ is expected to be twice $F^{xx}(1, \beta)$, if only contributions from magnetic atoms on the (0,0) column are taken into account. The discrepancy from this value is due to atoms on neighboring columns.

More precisely, we can write $\frac{\tilde{S}^z(1,\beta)}{F^{xx}(1,\beta)} = \frac{\tilde{S}^z_0(1,\beta) + \tilde{S}^z_{NC}(1,\beta)}{F^{xx}{}_0(1,\beta) + F^{xx}{}_{NC}(1,\beta)}$, where the subscript "*NC*" refers to contributions from columns (containing magnetic atoms) different from that at (0,0), whereas "*0*" refers to terms deriving from atoms on the (0,0) column. With reference to the trends observed for $\frac{F^{zz}(1,\beta)}{F^{xx}(1,\beta)}$, we expect that for a strongly channeling beam $|\tilde{S}^z_0(1, \beta)| \gg |\tilde{S}^z_{NC}(1, \beta)|$ and $F^{xx}{}_0(1, \beta) \gg F^{xx}{}_{NC}(1, \beta)$ and we can Taylor expand the ratio as $\frac{\tilde{S}^z(1,\beta)}{F^{xx}(1,\beta)} \approx \frac{\tilde{S}^z_0(1,\beta)}{F^{xx}{}_0(1,\beta)}[1 + \frac{\tilde{S}^z_{NC}(1,\beta)}{\tilde{S}^z_0(1,\beta)} - \frac{F^{xx}{}_{NC}(1,\beta)}{F^{xx}{}_0(1,\beta)}]$. The second and third terms in the square brackets, which are expected to be much smaller than unity, represent terms coming from neighboring columns and are responsible for the discrepancy from the expected value of -2 given by the ratio $\frac{\tilde{S}^z_0(1,\beta)}{F^{xx}{}_0(1,\beta)}$. The stronger is the channeling, the smaller in modulus are the values of the "*NC*" terms and the closer to -2 is this ratio. This is the reason why such a ratio is expected to be on average closer to -2 for FePt than for hcp cobalt. For an appropriate choice of collection angle β, this error can be reduced to below 5% for both of the considered sample thicknesses. We now investigate how the dichroism strength changes on varying the sample thickness in these two cases.

As an example, we fix a reasonable value of β, e.g., 12 mrad, and calculate $\frac{\tilde{S}^z(1,\beta)}{F^{xx}(1,\beta)}$ for different sample thicknesses. We find that for cobalt the ratio changes from -1.92 to -1.89 from a 20 nm to a 40 nm sample, with an associated decrease in relative dichroism signal of less than 2%. For FePt, this variation is much smaller (below 1%).

The relative dichroism function that is accessible using OAM-resolved EMCD for samples with these rotational symmetries is therefore only very weakly dependent on dynamical diffraction, in contrast to the situation for conventional EMCD. For comparison, we underline here that the fact that calculations performed by Rusz *et al.* [8] predict a variation in dichroism for hcp cobalt of ∼80% on changing the sample thickness from 20 to 40 nm.

The physical reason for this difference is that, for the present experimental setup, the term $\frac{\tilde{S}^z(1,\beta)}{F^{xx}(1,\beta)}$ is determined mainly by the inelastic signal from the magnetic atoms in the

column on which the probe is located, which is thickness-independent and is determined only by symmetry for $\frac{\pi}{2}$ and $\frac{2\pi}{3}$ rotationally invariant crystals.

Changes from these limiting values are thickness-dependent, but are generally a small fraction of the value determined by the atoms at (0,0).We have shown that their strengths are determined by inelastic excitations occurring on neighboring columns. They can therefore be controlled by using a STEM probe that exhibits strong channeling along the atomic column on which the probe is located, suggesting a possible way to further reduce this discrepancy by smart engineering of the channeling properties of the incoming electron beam. As pointed out in Ref. [16], the use of a Gaussian beam with a transverse size comparable to the $1s$ Bloch state associated with the atomic column on which this probe is focused could strongly enhance the channeling capability of the beam, thereby reducing the number of inelastic excitations occurring on neighboring columns, which are responsible for the observed discrepancies.

In Appendix C, we demonstrate that, for these systems, the orbital and spin components of the atomic magnetic moments can be written as $m_{\rm orb} = C_{\rm orb}(\frac{\tilde{S}^z(1,\beta)}{F^{xx}(1,\beta)})^{-1}$ and $m_s = C_s(\frac{\tilde{S}^z(1,\beta)}{F^{xx}(1,\beta)})^{-1}$, where $C_{\rm orb}$ and C_s depend on experimentally accessible spectra and material-specific terms. [Their extended expressions are provided in Eqs. (C14) and (C15).]

As we have demonstrated that $(\frac{\tilde{S}^z(1,\beta)}{F^{xx}(1,\beta)})^{-1}$ is only slightly dependent on β, an approximate evaluation of $m_{\rm orb}$ and m_S can be obtained directly from experimentally measured spectra by approximating $(\frac{\tilde{S}^z(1,\beta)}{F^{xx}(1,\beta)})^{-1}$ by the limiting value of -0.5, assuming a probe that exhibits good channeling properties. An estimate of the error associated with this approximation requires dynamical diffraction calculations similar to those reported in this work. However, we expect the error to be within experimental uncertainty if an appropriate choice of β is made.

V. CONCLUSIONS

In this work, we have provided relations between dynamical coefficients appearing in STEM OAM-resolved energy-loss spectra, for a convergent electron beam that is focused on an atomic column that is a rotational symmetry axis for the crystal. Some of the relations are valid in a general context and depend only on the zone axis symmetry of the crystal, while some of them require strong channeling of the probe on an atomic column.

We have also shown that, for the present cases and experimental conditions, the dichroism spectrum that is accessible using this technique is only slightly dependent on dynamical diffraction effects and is therefore almost independent of sample thickness. This is a great advantage when compared with the original setup proposed for electron energy-loss magnetic chiral dichroism. It could open the way to the reliable determination of the orbital and spin components of atomic magnetic moments directly from experimental spectra.

ACKNOWLEDGMENTS

This work is supported by Q-SORT, a project funded by the 484 European Union's Horizon 2020 Research and Innovation 485 Program under Grant agreement No. 766970. This project has received funding from the European Research Council (ERC) under the European Union's Horizon 2020 research and innovation programme (Grant No. 856538, project "3D MAGiC"), from the European Union's Horizon 2020 Research and Innovation Programme (Grant No. 823717, project "ESTEEM3"), from the DARPA TEE program through Grant MIPR No. HR0011831554 and from the Deutsche Forschungsgemeinschaft (DFG, German Research Foundation), Project ID No. 405553726 - TRR 270. E.K. acknowledges the support of Canada Research Chair (CRC), and Early Research Award (ERA).

APPENDIX A: CONTRIBUTIONS TO DYNAMICAL COEFFICIENTS DUE TO ATOMS NOT ON THE (0,0) COLUMN: THE CASE OF $\frac{\pi}{2}$ AND π ROTATIONALLY INVARIANT CRYSTALS

We start from the case of π rotationally invariant crystals. In this case, given an atom $\boldsymbol{a}_0$ out of away from the (0,0) column, we have another atom $\boldsymbol{a}_1 = \overline{\overline{A}}\,\boldsymbol{a}_0$, where $\overline{\overline{A}}$ describes a π rotation around the z axis. If we use Eq. (3.5), we have

$$\begin{aligned}\boldsymbol{Q}(\ell,k;\boldsymbol{a}_1) &= e^{i\ell\pi}[\overline{\overline{A}}_0^{-1}\boldsymbol{Q}(\ell,k;\overline{\overline{A}}\,\boldsymbol{a}_1)]\\ &= e^{i\ell\pi}[\overline{\overline{A}}_0^{-1}\boldsymbol{Q}(\ell,k;\overline{\overline{A}}\,\overline{\overline{A}}\,\boldsymbol{a}_0)]\\ &= e^{i\ell\pi}[\overline{\overline{A}}_0^{-1}\boldsymbol{Q}(\ell,k;\boldsymbol{a}_0)],\end{aligned}$$

where the relation $\overline{\overline{A}}\,\overline{\overline{A}} = 1$, which is valid for π matrix rotation, is used. For $\ell = \pm 1$, we obtain

$$Q_x(\ell,k;\boldsymbol{a}_1) = Q_x(\ell,k;\,\boldsymbol{a}_0),$$

$$Q_y(\ell,k;\boldsymbol{a}_1) = Q_y(\ell,k;\,\boldsymbol{a}_0),$$

$$Q_z(\ell,k;\boldsymbol{a}_1) = -Q_z(\ell,k;\,\boldsymbol{a}_0).$$

We can now compute the sum of the contributions to the different dynamical coefficients of these two equivalent atoms, i.e.,

$$\sum_{\boldsymbol{a}\in\{\boldsymbol{a}_0,\boldsymbol{a}_1\}} |Q_x(\ell,k;\boldsymbol{a})|^2 = 2|Q_x(\ell,k;\boldsymbol{a}_0)|^2, \tag{A1}$$

$$\sum_{\boldsymbol{a}\in\{\boldsymbol{a}_0,\boldsymbol{a}_1\}} |Q_y(\ell,k;\boldsymbol{a})|^2 = 2|Q_y(\ell,k;\boldsymbol{a}_0)|^2, \tag{A2}$$

$$\sum_{\boldsymbol{a}\in\{\boldsymbol{a}_0,\boldsymbol{a}_1\}} |Q_z(\ell,k;\boldsymbol{a})|^2 = 2|Q_z(\ell,k;\boldsymbol{a}_0)|^2, \tag{A3}$$

$$\sum_{\boldsymbol{a}\in\{\boldsymbol{a}_0,\boldsymbol{a}_1\}} Q_x(\ell,k;\boldsymbol{a})Q^*{}_y(\ell,k;\boldsymbol{a}) = 2Q_x(\ell,k;\boldsymbol{a}_0)Q^*{}_y(\ell,k;\boldsymbol{a}_0), \tag{A4}$$

$$\sum_{\boldsymbol{a}\in\{\boldsymbol{a}_0,\boldsymbol{a}_1\}} Q_i(\ell,k;\boldsymbol{a})Q^*{}_z(\ell,k;\boldsymbol{a}) = 0. \tag{A5}$$

From Eqs. (A1) and (A2), the contributions to X^{xx} and X^{yy} are different, as $Q_x(\ell,k;\boldsymbol{a}_0)$ is in general different from $Q_y(\ell,k;\boldsymbol{a}_0)$, while Eq. (A3) indicates that, as for $\frac{2\pi}{3}$ rotationally invariant systems, the terms associated with X^{zz}, which are obtained from equivalent atoms, sum together in phase.

The same situation occurs for the summation in Eq. (A4), which represents contributions to the functions X^{xy} and S^z. [In order to obtain these functions, it is necessary to extract the real and imaginary parts of Eq. (A4).] Equation (A5) indicates that for $i = x, y$, the contributions of these equivalent atoms to the cross terms X^{xz} and X^{yz} exactly cancel out. This means that π rotational symmetry around z guarantees that F^{xz} and F^{yz} are zero, whereas F^{zz} is expected to be different from zero, but its value is only determined by contributions from magnetic atoms on columns that are different from that at (0,0).

We now focus our attention to the case of $\frac{\pi}{2}$ rotationally invariant systems. In these crystals, there are four equivalent atoms, which can be related to each other through $\frac{\pi}{2}$ rotations around the z axis, i.e., $\boldsymbol{a}_0, \boldsymbol{a}_1 = \bar{\bar{A}}\boldsymbol{a}_0, \boldsymbol{a}_2 = \bar{\bar{A}}\boldsymbol{a}_1$ and $\boldsymbol{a}_3 = \bar{\bar{A}}\boldsymbol{a}_2$, with $\boldsymbol{a}_0 = \bar{\bar{A}}\boldsymbol{a}_3$.

Exploiting Eq. (3.5), we obtain

$$\begin{aligned}
\boldsymbol{Q}(\ell,k;\boldsymbol{a}_1) &= e^{i\ell\frac{\pi}{2}}[\bar{\bar{A}}_0^{-1}\boldsymbol{Q}(\ell,k;\bar{\bar{A}}\boldsymbol{a}_1)] = e^{i\ell\frac{\pi}{2}}[\bar{\bar{A}}_0^{-1}\boldsymbol{Q}(\ell,k;\boldsymbol{a}_2)] \\
&= e^{i\ell\pi}[\bar{\bar{A}}_0^{-1}\bar{\bar{A}}_0^{-1}\boldsymbol{Q}(\ell,k;\bar{\bar{A}}\boldsymbol{a}_2)] \\
&= e^{i\ell\pi}\bar{\bar{A}}_0^{-1}\bar{\bar{A}}_0^{-1}\boldsymbol{Q}(\ell,k;\boldsymbol{a}_3) \\
&= e^{i\ell\frac{3\pi}{2}}\bar{\bar{A}}_0^{-1}\bar{\bar{A}}_0^{-1}\bar{\bar{A}}_0^{-1}\boldsymbol{Q}(\ell,k;\boldsymbol{a}_0), \\
\boldsymbol{Q}(\ell,k;\boldsymbol{a}_2) &= e^{i\ell\frac{\pi}{2}}[\bar{\bar{A}}_0^{-1}\boldsymbol{Q}(\ell,k;\bar{\bar{A}}\boldsymbol{a}_2)] \\
&= e^{i\ell\frac{\pi}{2}}[\bar{\bar{A}}_0^{-1}\boldsymbol{Q}(\ell,k;\boldsymbol{a}_3)] = e^{i\ell\pi}\bar{\bar{A}}_0^{-1}\bar{\bar{A}}_0^{-1}\boldsymbol{Q}(\ell,k;\boldsymbol{a}_0) \\
\boldsymbol{Q}(\ell,k;\boldsymbol{a}_3) &= e^{i\ell\frac{\pi}{2}}[\bar{\bar{A}}_0^{-1}\boldsymbol{Q}(\ell,k;\bar{\bar{A}}\boldsymbol{a}_3)] = e^{i\ell\frac{\pi}{2}}\bar{\bar{A}}_0^{-1}\boldsymbol{Q}(\ell,k;\boldsymbol{a}_0),
\end{aligned}$$

i.e., we can write the functions $\boldsymbol{Q}(\ell,k;\boldsymbol{a})$ for all four equivalent atoms in terms of those evaluated for only one of them. By using these relations, we can compute the sum of the contributions to the dynamical coefficients for these atoms, i.e.,

$$\sum_{\boldsymbol{a}\in\{\boldsymbol{a}_0,\boldsymbol{a}_1,\boldsymbol{a}_2,\boldsymbol{a}_3\}} |Q_x(\ell,k;\boldsymbol{a})|^2 = 2|Q_x(\ell,k;\boldsymbol{a}_0)|^2 + 2|Q_y(\ell,k;\boldsymbol{a}_0)|^2, \tag{A6}$$

$$\sum_{\boldsymbol{a}\in\{\boldsymbol{a}_0,\boldsymbol{a}_1,\boldsymbol{a}_2,\boldsymbol{a}_3\}} |Q_y(\ell,k;\boldsymbol{a})|^2 = 2|Q_x(\ell,k;\boldsymbol{a}_0)|^2 + 2|Q_y(\ell,k;\boldsymbol{a}_0)|^2, \tag{A7}$$

$$\sum_{\boldsymbol{a}\in\{\boldsymbol{a}_0,\boldsymbol{a}_1,\boldsymbol{a}_2,\boldsymbol{a}_3\}} |Q_z(\ell,k;\boldsymbol{a})|^2 = 4|Q_z(\ell,k;\boldsymbol{a}_0)|^2, \tag{A8}$$

$$\sum_{\boldsymbol{a}\in\{\boldsymbol{a}_0,\boldsymbol{a}_1,\boldsymbol{a}_2,\boldsymbol{a}_3\}} Q_x(\ell,k;\boldsymbol{a})Q^*{}_y(\ell,k;\boldsymbol{a}) = 4i\mathrm{Im}[Q_x(\ell,k;\boldsymbol{a}_0)Q^*{}_y(\ell,k;\boldsymbol{a}_0)], \tag{A9}$$

$$\sum_{\boldsymbol{a}\in\{\boldsymbol{a}_0,\boldsymbol{a}_1,\boldsymbol{a}_2,\boldsymbol{a}_3\}} Q_i(\ell,k;\boldsymbol{a})Q^*{}_z(\ell,k;\boldsymbol{a}) = 0 \; for \; i = x, y. \tag{A10}$$

Equations (A6) and (A7) show that the contributions X^{xx} and X^{yy} due to these equivalent atoms are the same. Therefore, we have $F^{xx} = F^{yy}$ for $\ell = \pm 1$. As in the two previous cases, the contributions to X^{zz} due to the equivalent atoms sum in phase [see Eq. (A8)], while Eq. (A9) indicates that the sum of the terms $Q_x(\ell,k;\boldsymbol{a})Q^*{}_y(\ell,k;\boldsymbol{a})$ has no real part, so that we have $X^{xy} = 0$. However, the imaginary parts sum in phase and so a nonzero contribution to S^z due to the atoms not on (0,0) is expected.

Finally, Eq. (A10) shows that the cross terms X^{xz} and X^{yz} are zero because contributions from the atoms on columns different from that at (0,0) sum destructively.

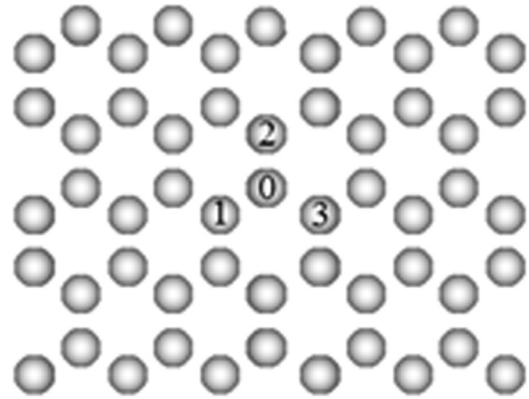

FIG. 5. hcp cobalt viewed along the [001] direction. Columns denoted c_1, c_2, c_3 are formed from atoms that can be obtained from each other through rotations of $2\pi/3$ around the column denoted c_0, where the STEM probe is located.

APPENDIX B: CONTRIBUTIONS TO DYNAMICAL COEFFICIENTS FROM MAGNETIC ATOMS ON COLUMNS THAT ARE NEAREST NEIGHBORS TO THAT AT (0,0) FOR $\frac{2\pi}{3}$ ROTATIONALLY INVARIANT CRYSTALS: [001] HCP COBALT

In this section, we demonstrate Eq. (3.9) derived in the main text, focusing on contributions to the different dynamical coefficients due to equivalent atoms on nearest neighboring columns to that at (0,0) on which the probe is located, for [001] hcp cobalt.

More precisely, we display the quantities

$$F^{ij}_{\boldsymbol{a}}(\ell = 1, \beta) = \int_0^{\frac{2\pi\beta}{\lambda}} X^{ij}_{\boldsymbol{a}}(\ell = 1, k)kdk \tag{B1}$$

for atoms $\boldsymbol{a}$ on three nearest neighboring columns indicated in Fig. 5 as c_1, c_2, c_3. The results are presented for these equivalent atoms (which can be obtained from each other through $\frac{2\pi}{3}$ rotations) and can be extended to further columns once equivalent atoms are taken into account. Column c_0 in Fig. 5 corresponds to that on which the probe is focused.

In the following, the collection semiangle β will be kept fixed to a reasonable value of 11 mrad and we focus on a cobalt sample with a thickness of 20 nm.

Figure 6 shows the quantities defined in Eq. (B1) for a probe with a convergence semiangle of 7 mrad. We note here that Eqs (3.9) (just as those found in Appendix A) are independent of the probe convergence semiangle. We show in Fig. 7 how these dynamical coefficients computed for atoms not on (0,0) change by increasing the probe convergence semiangle, i.e., by adopting a probe with stronger channeling properties.

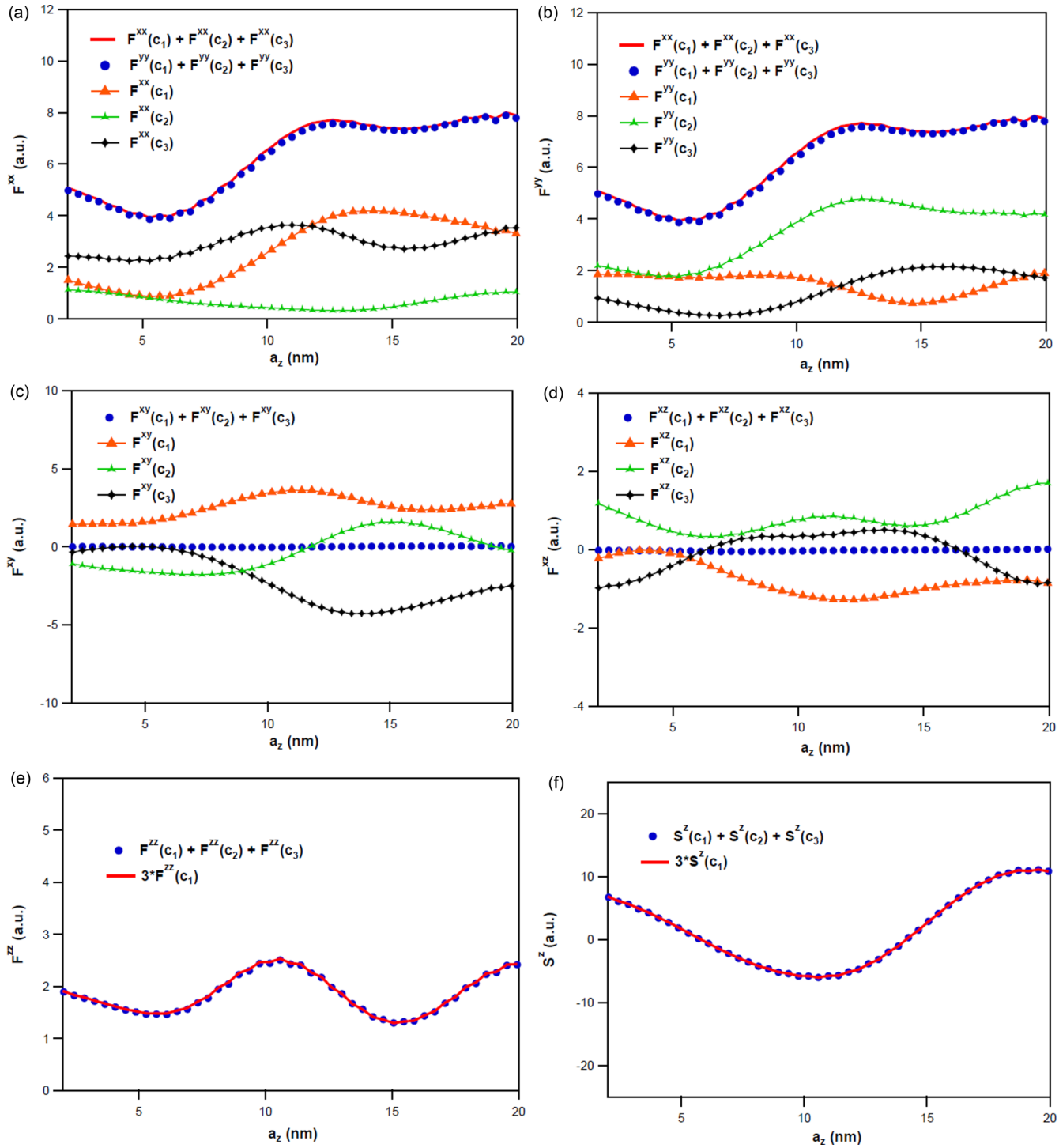

FIG. 6. Contributions to the dynamical coefficients F^{ij} and $\tilde{S}^z$ due to the atoms of the three columns indicated in Fig. 5. The calculations have been performed for a 20-nm-thick cobalt crystal, assuming convergence semiangle of 7 mrad and integrating the final signal up to a collection semiangle of 11 mrad.

Figures 6(a) and 6(b) show the functions $F_{\boldsymbol{a}}^{xx}(\ell = 1, \beta)$ and $F_{\boldsymbol{a}}^{yy}(\ell = 1, \beta)$, respectively, for atoms $\boldsymbol{a}$ along columns c_1, c_2, c_3 indicated in Fig. 5. On both graphs, we also show the sum of the contributions to F^{xx} and F^{yy}. We notice that, despite the fact that the contributions to F^{xx} and F^{yy} from atoms on different columns are different, the sums $\sum_{\boldsymbol{a}\in\{c_1,c_2,c_3\}} F_{\boldsymbol{a}}^{xx}$ and $\sum_{\boldsymbol{a}\in\{c_1,c_2,c_3\}} F_{\boldsymbol{a}}^{yy}$ are the same.

Figures 6(c) and 6(d) show the functions $F_{\boldsymbol{a}}^{xy}(\ell = 1, \beta)$ and $F_{\boldsymbol{a}}^{xz}(\ell = 1, \beta)$, respectively, together with the sums $\sum_{\boldsymbol{a}\in\{c_1,c_2,c_3\}} F_{\boldsymbol{a}}^{xy}$ and $\sum_{\boldsymbol{a}\in\{c_1,c_2,c_3\}} F_{\boldsymbol{a}}^{xz}$. Just as predicted by Eqs. (3.9b) and (3.9d), the contributions to these functions from rotationally equivalent atoms cancel each other out.

Finally, Figs. 6(e) and 6(f) show $\sum_{\boldsymbol{a}\in\{c_1,c_2,c_3\}} F_{\boldsymbol{a}}^{zz} = 3F_{\boldsymbol{a}\in c_1}^{zz}$ and $\sum_{\boldsymbol{a}\in\{c_1,c_2,c_3\}} \tilde{S}_{\boldsymbol{a}}^{z} = 3\tilde{S}_{\boldsymbol{a}\in c_1}^{z}$.

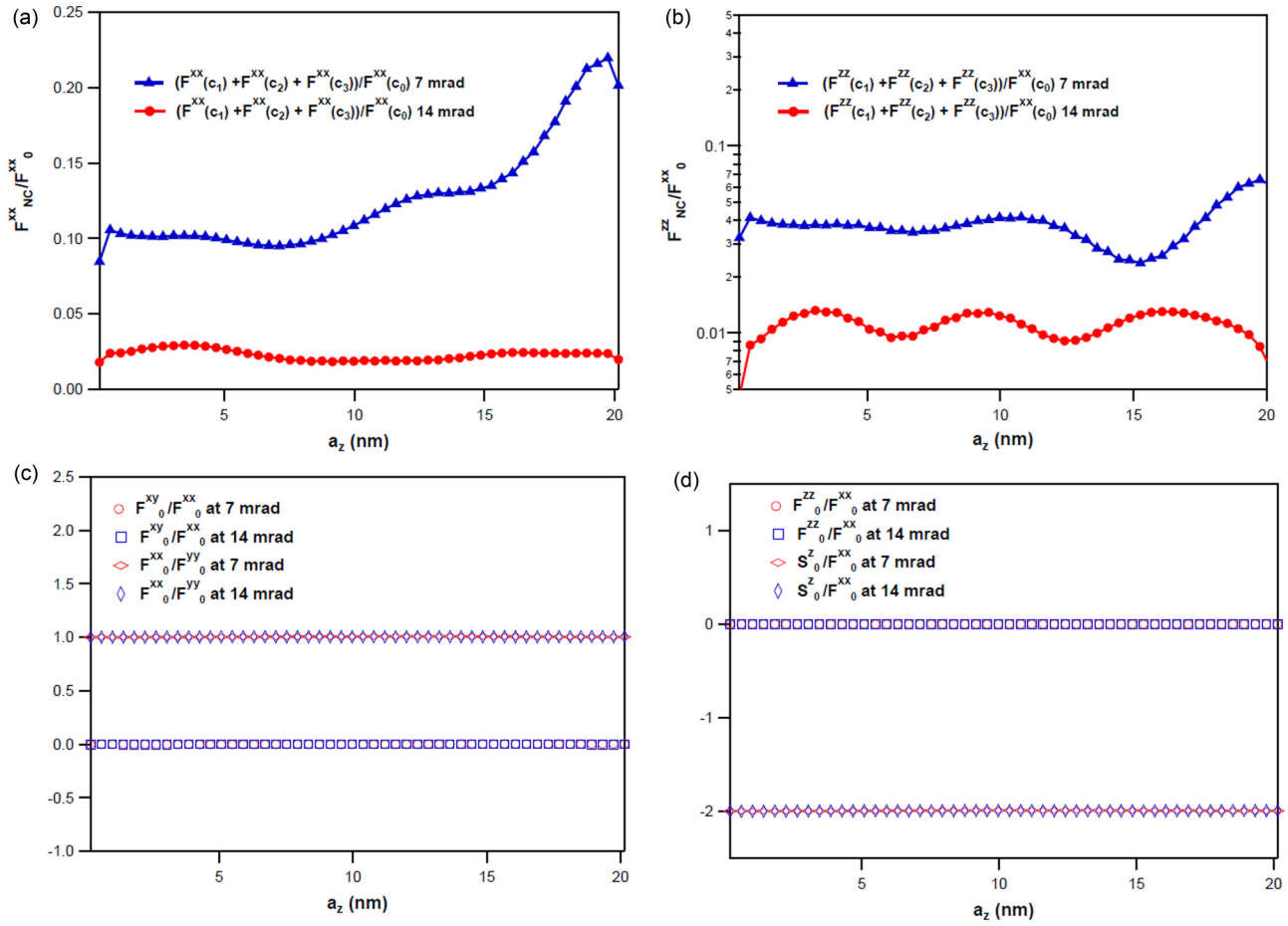

FIG. 7. (a) Ratios between contributions from columns c_1 c_2 and c_3 and the c_0 column to F^{xx} are shown for two different convergence semiangles of the STEM probe. (b) Contributions of the neighboring columns to F^{zz} are compared with F^{xx} associated with the (0,0) column. The subscript "NC" refers to neighboring columns, while the subscript "0" refers to the (0,0) column on which the probe is focused. (c) and (d) show Eq. (3.7a), (3.7b), (3.7d) and (3.7e) in the main text tested for convergence semiangles of 7 and 14 mrad.

In order to complete the analysis of the contributions from atoms on neighboring columns, Figs. 7(a) and 7(b) show the ratios $\frac{\sum_{\boldsymbol{a}\in\{c_1,c_2,c_3\}} F^{xx}_{\boldsymbol{a}}}{F^{xx}_{(0,0)}}$, $\frac{\sum_{\boldsymbol{a}\in\{c_1,c_2,c_3\}} F^{zz}_{\boldsymbol{a}}}{F^{xx}_{(0,0)}}$ computed for STEM probes of 7 and 14 mrad. An increase in the probe convergence semiangle decreases these ratios, as for the second probe the incoming electron beam exhibits stronger channeling along the atomic column on which it is focused, so the number of inelastic events occurring on columns c_1, c_2 and c_3 is decreased and correspondingly also $\sum_{\boldsymbol{a}\in\{c_1,c_2,c_3\}} F^{xx}_{\boldsymbol{a}}$ and $\sum_{\boldsymbol{a}\in\{c_1,c_2,c_3\}} F^{zz}_{\boldsymbol{a}}$ decrease. Finally in Fig. 7(c) we show the functions $\frac{F^{xx}_{\boldsymbol{a}}}{F^{yy}_{\boldsymbol{a}}}$ and $\frac{F^{xy}_{\boldsymbol{a}}}{F^{xx}_{\boldsymbol{a}}}$, while in Fig. 7(d) we show $\frac{\tilde{S}^{z}_{\boldsymbol{a}}}{F^{xx}_{\boldsymbol{a}}}$ and $\frac{F^{zz}_{\boldsymbol{a}}}{F^{xx}_{\boldsymbol{a}}}$ computed, in both cases for atoms $\boldsymbol{a}$ on the (0,0) column for two different convergence semiangles. Relations between the dynamical coefficients computed for atoms at (0,0) are effectively independent from the probe convergence semiangle.

APPENDIX C: CONNECTION BETWEEN OAM-RESOLVED EMCD SPECTRA AND m_{orb}, m_s

In this section, we derive an expression that connects m_{orb}, m_s with measured OAM-resolved loss spectra for cases when Eq. (4.1) in the main text provides a good approximation for OAM-resolved loss spectra. The sample is always assumed to be fully polarized along the z axis.

As a first point, we need to find a relation between $M(\Delta E)$, $N_{ii}(\Delta E)$ (integrated over the atomic edges L_2 and L_3) and the orbital and spin components of the atomic magnetic moment, starting from the equations provided in Ref. [5]. The main steps that are necessary to find these relations are as follows.

We define

$$M(L_2;L_3) = \int_{L_2+L_3} M(\Delta E)d\Delta E, \tag{C1}$$

$$M(L_2) = \int_{L_2} M(\Delta E)d\Delta E, \tag{C2}$$

$$M(L_3) = \int_{L_3} M(\Delta E)d\Delta E, \tag{C3}$$

i.e., the integral over the edges L_2 and L_3 of the energy-dependent imaginary part of the mixed dynamic form factor.

Starting from Eq. (4) in Ref. [5], we have the expression

$$M(L_2;L_3) = \frac{1}{2}\frac{9G}{(2L+1)\mu_B} m_{orb}, \tag{C4}$$

where the orbital component of the atomic magnetic moment is given by $m_{\rm orb} = \mu_B \langle \boldsymbol{L} \rangle_z$ and $\langle \boldsymbol{L} \rangle_z$ is the expectation value of the atomic OAM along the z axis. This is correct only if the sample is fully magnetized along z. G is a positive quantity, which depends only on the material electronic properties and can be computed applying the dipolar approximation to Eq. (5) of Ref. [5]. The index L is equal to 2 for *3d* transition metal atoms.

At the same time, we can exploit Eq. (6) of Ref. [5] to evaluate the integral of $M(\Delta E)$ over the two distinct atomic edges, i.e., $M(L_2)$ and $M(L_3)$. In practice,

$$M(L_2) = \frac{9G}{(2L-1)(2L+1)}\left[\frac{L-1}{2}\langle \boldsymbol{L} \rangle_z - \frac{\langle \boldsymbol{S} \rangle_z (L-1)L}{3}\left(1 + \frac{2L+3}{L}\frac{\langle \boldsymbol{T} \rangle_z}{\langle \boldsymbol{S} \rangle_z}\right)\right], \tag{C5}$$

$$M(L_3) = \frac{9G}{(2L-1)(2L+1)}\left[\frac{L}{2}\langle \boldsymbol{L} \rangle_z + \frac{\langle \boldsymbol{S} \rangle_z (L-1)L}{3}\left(1 + \frac{2L+3}{L}\frac{\langle \boldsymbol{T} \rangle_z}{\langle \boldsymbol{S} \rangle_z}\right)\right], \tag{C6}$$

where $\langle \boldsymbol{S} \rangle_z$ is the expectation value of the atomic spin along the z axis. As pointed out by Chen *et al.* [17], the ratio $\frac{\langle \boldsymbol{T} \rangle_z}{\langle \boldsymbol{S} \rangle_z}$ is generally negligible for bulk systems, so we neglect this quantity below. Exploiting Eq. (C5) and Eq. (C6), we write

$$\frac{1}{L}M(L_3) - \frac{1}{L-1}M(L_2) = \frac{3G}{\mu_B(2L+1)}m_s. \tag{C7}$$

Finally, by using Eq. (8) of Ref. [5], which provides a sum rule for the real part of the mixed dynamic form factor, it is possible to obtain an expression for the integral of $N_{ii}(\Delta E)$ over the two edge in the form

$$\int_{L_2+L_3} N_{ii}(\Delta E)\Delta E = \frac{9L^2 G}{(2L-1)(2L+1)}D_{ii}, \tag{C8}$$

where D_{ii} (for $i = x, y$) are quantities that are again only dependent on the electronic properties of the material, which can be evaluated using *ab initio* calculations.

We now use Eq. (4.1) from the main text for the OAM loss spectrum, with the additional assumption that the crystal under study has a mirror plane containing the z axis. In this case, we can write

$$I_\beta(\ell = +1, \Delta E) + I_\beta(\ell = -1, \Delta E) = 2[N_{xx}(\Delta E) + N_{yy}(\Delta E)]F^{xx}(\ell = +1, \beta), \tag{C9}$$

$$I_\beta(\ell = +1, \Delta E) - I_\beta(\ell = -1, \Delta E) = 2M(\Delta E)\tilde{S}^z(\ell = +1, \beta), \tag{C10}$$

and for the corresponding quantities integrated over the atomic edges we have

$$A(L_2; L_3) = \int_{L_2+L_3} [I_\beta(\ell = +1, \Delta E) + I_\beta(\ell = -1, \Delta E)]d\Delta E, \tag{C11}$$

$$A(L_2) = \int_{L_2} [I_\beta(\ell = +1, \Delta E) - I_\beta(\ell = -1, \Delta E)]d\Delta E, \tag{C12}$$

$$A(L_3) = \int_{L_3} [I_\beta(\ell = +1, \Delta E) - I_\beta(\ell = -1, \Delta E)]d\Delta E, \tag{C13}$$

Therefore, by combining Eqs. (C9), (C10), (C11), (C12) and (C13) with Eqs. (C4), (C7), and (C8), it is possible to find that

$$m_{\rm orb} = \left[\frac{2(D_{xx} + D_{yy})L^2\mu_B}{2L-1}\right]\left[\frac{A(L_2) + A(L_3)}{A(L_2; L_3)}\right]\frac{F^{xx}(\ell = +1, \beta)}{\tilde{S}^z(\ell = +1, \beta)}, \tag{C14}$$

$$m_s = \left[\frac{3(D_{xx} + D_{yy})L^2\mu_B}{2L-1}\right]\left[\frac{\frac{1}{L}A(L_3) - \frac{1}{L-1}A(L_2)}{A(L_2; L_3)}\right]\frac{F^{xx}(\ell = +1, \beta)}{\tilde{S}^z(\ell = +1, \beta)}. \tag{C15}$$

In Eqs. (C14) and (C15), the first term on the r.h.s depends only on the material electronic properties, the second can be found directly from experimental OAM resolved energy-integrated EMCD spectra, while the third, i.e., the ratio $\frac{F^{xx}(\ell=+1,\beta)}{\tilde{S}^z(\ell=+1,\beta)}$, describes the dependence on dynamical diffraction effects.

[1] P. Schattschneider, S. Rubino, C. Hebert, J. Rusz, J. Kunes, P. Novak, E. Carlino, M. Fabrizioli, G. Panaccione, and G. Rossi, Nature (London) **441**, 486 (2006).

[2] B. T. Thole, P. Carra, F. Sette, and G. van der Laan, Phys. Rev. Lett. **68**, 1943 (1992).

[3] P. Carra, B. T. Thole, M. Altarelli, and X. Wang, Phys. Rev. Lett. **70**, 694 (1993).

[4] L. Calmels, F. Houdellier, B.Warot-Fonrose, C. Gatel, M. J. Hytch, V. Serin, E. Snoeck, and P. Schattschneider, Phys. Rev. B **76**, 060409(R) (2007).

[5] J. Rusz, O. Eriksson, P. Novak, and P. M. Oppeneer, Phys. Rev. B **76**, 060408(R) (2007).
[6] E. Rotunno, M. Zanfrognini, S. Frabboni, J. Rusz, R. E. Dunin Borkowski, E. Karimi, and V. Grillo, Phys. Rev. B **100**, 224409 (2019).
[7] V. Grillo, A. H. Tavabi, F. Venturi, H. Larocque, R. Balboni, G. C. Gazzadi, S. Frabboni, P. H. Lu, E. Mafakheri, F. Bouchard, R. E. Dunin-Borkowski, R. W. Boyd, M. P. J. Lavery, M. J. Padgett, and E. Karimi, Nat. Commun. **8**, 15536 (2017).
[8] J. Rusz, S. Rubino, and P. Schattschneider, Phys. Rev. B **75**, 214425 (2007).
[9] M. Zanfrognini, E. Rotunno, S. Frabboni, A. Sit, E. Karimi, U. Hohenester, and V. Grillo, ACS Photonics, **6**, 620 (2019).
[10] J. Rusz, A. Lubk, J. Spiegelberg, and D. Tyutynnikov, Phys. Rev. B **96**, 245121 (2017).
[11] T.Schachinger, S. Löffler, A. Steiger-Thirsfeld, M. Stöger-Pollach, S. Schneider, D. Pohl, B. Rellinghaus, and P. Schattschneider, Ultramicroscopy **179**, 15 (2017).
[12] M. V. Vasnetsov, V. A. Pasko, and M. S. Soskin, New J. Phys. **7**, 46 (2005).
[13] P. Schattschneider, S. Löffler, M. Stöger-Pollach, and J. Verbeeck, Ultramicroscopy **136**, 81 (2014).
[14] J. Rusz, Ultramicroscopy **177**, 20 (2017).
[15] See Supplemental Material at http://link.aps.org/supplemental/10.1103/PhysRevB.102.184420 for the analysis of dynamical diffraction coefficients in crystals with different symmetries.
[16] E. Rotunno, A. H. Tavabi, E. Yucelen, S. Frabboni, R. E. Dunin Borkowski, E. Karimi, B. J. McMorran, and V. Grillo, Phys. Rev. Appl. **11**, 044072 (2019).
[17] C. T. Chen, Y. U. Idzerda, H.-J. Lin, N. V. Smith, G. Meigs, E. Chaban, G. H. Ho, E. Pellegrin, and F. Sette, Phys. Rev. Lett. **75**, 152 (1995).